Sub-ice shelf sediments record 20th Century retreat history of Pine Island Glacier

Smith, J.A[1*]., Andersen, T.J[2]., Shortt, M[1]., Gaffney, A.M[3]., Truffer, M[4]., Stanton, T.P[5]., Bindschadler, R[6]., Dutrieux, P[7]., Jenkins, A[1]., Hillenbrand, C.-D[1]., Ehrmann, W[8]., Corr, H.F.J[1]., Farley, N[1,9]., Crowhurst, S[9]., Vaughan, D.G[1].

[1]British Antarctic Survey, Cambridge, CB3 0ET, UK.

[2]Center for permafrost (CENPERM), Department of Geosciences and Natural Resource Management, University of Copenhagen, 1350 Copenhagen K, Denmark.

[3]Nuclear and Chemical Science Division, Lawrence Livermore National Laboratory, Livermore, CA 94550-9234, USA.

[4]Geophysical Institute, University of Alaska, Fairbanks, AK 99775–7320, USA.

[5]Department of Oceanography, Naval Postgraduate School, Monterey, CA 93943, USA.

[6]Emeritus Scientist, NASA Goddard Space Flight Center, Greenbelt, MD 20771, USA.[7]Lamont-Doherty Earth Observatory of Columbia University, Palisades, New York 10964, USA.

[8]Institute for Geophysics and Geology, University of Leipzig, Talstrasse 35, D-04103 Leipzig, Germany.

[9]University of Geneva, Department of Earth Sciences, 13 Rue des Maraîchers, 1205 Geneva, Switzerland.

[10]Godwin Laboratory for Palaeoclimate Research, Department of Earth Sciences, University of Cambridge, Downing Street, Cambridge CB2 3EQ, UK.

*Corresponding author. Email: jaas@bas.ac.uk

The West Antarctic Ice Sheet represents one of the largest potential sources of future sea-level rise1. Over the past 40 years, glaciers flowing into the Amundsen Sea sector of the ice sheet have thinned at an accelerating rate[2], and several numerical models now suggest that unstable and irreversible grounding line retreat is underway[3]. Understanding the controls on recent retreat requires a detailed understanding of grounding line history[4], but former positions are poorly dated prior to the advent of satellite monitoring in the 1990s. The grounding line retreat history is required to address the relative roles of contemporaneous ocean forcing and ongoing glacier response to an earlier perturbation in driving ice sheet loss. Here we show that the present thinning and retreat of Pine Island Glacier is part of a climatically forced trend triggered in the 1940s. Our conclusions arise from sediment cores recovered beneath the floating Pine Island Glacier ice shelf, and constrain the pre-satellite timing of grounding-line retreat from a prominent sea-floor ridge. Incursion of marine water beyond the ridge crest occurred in 1945 ± 12 years at the latest and final ungrounding of the ice shelf from the ridge in 1970 ± 4 years. Initial opening of the current sub-ice shelf ocean cavity in the mid-1940s followed a period of strong warming of West Antarctica associated with El Niño activity, implying that even when climate forcing weakened ice sheet retreat continued.

Pine Island Glacier (PIG, Fig. 1), which drains into the Amundsen Sea, has retreated continuously throughout the short observational record (1992-present)[2]. The coherent thinning of glaciers along the Amundsen Sea coast indicates a response to external forcing[8] and has been attributed to high basal melting of the floating ice shelves by warm Circumpolar Deep Water (CDW)[9]. Thinner ice shelves are less able to buttress inland ice, leading to glacier acceleration and ice sheet thinning[10,11].

Although the ocean has been identified as a key driver of recent ice sheet changes, the longer term context and specifically when the current imbalance was initiated, remains uncertain. Evidence gathered by Autosub, an autonomous under water vehicle operating beneath the ice shelf of PIG, revealed a prominent sea-floor ridge[12] which probably acted as the most recent steady grounding line (GL) position. The earliest visible satellite image from 1973 showed a bump on the ice surface that was interpreted as the last point of grounding on the highest part of the ridge[12,13]. The bump had disappeared several years later implying that the current phase of thinning was already underway at that time[12].

This provided the first suggestion that recent retreat could be part of a longer-term process which started decades or even centuries prior to satellite observations. On geological timescales the ice sheet extended up to, or very close to, the continental shelf edge in the eastern Amundsen Sea at the Last Glacial Maximum (LGM; 23-19 kyr ago), and retreat of the GL to a position close to the current calving margin was complete by 10 kyr[14]. Retreat of the PIG GL from this point to the ridge is not constrained but it is possible that the GL had retreated to the sea-floor ridge soon after 10 kyr and remained there until some recent, but currently undetermined time in the past.

On decadal timescales variability in the winds over the outer Amundsen Sea continental shelf, which are thought to drive changes in CDW delivery to Pine Island Bay[15], are linked to sea surface temperature variability in the central tropical Pacific[16]. Warm (El Niño) conditions in the central Pacific are thought to create warm oceanic conditions on the Amundsen Sea shelf and the same conditions drive atmospheric warming in West Antarctica[16]. The El Niño record includes a major central Pacific warm event in the early 1940s, and ice cores show that this was a time of exceptional warmth in West Antarctica[17].

The implication is that if conditions in the Amundsen Sea were anomalously warm in the past, this could have been the trigger for the current ice thinning. Recent work shows that cooler waters on the Amundsen shelf in 2012 coincided with La Niña conditions, providing observational support for the hypothesised link between conditions in the central Pacific and the Amundsen shelf where El Niño favours enhanced melting[16] and La Niña favours decreased melting[7].

However, with only a few decades of satellite data and no direct observations of GL retreat of PIG during the 20th century, it remains difficult to assess fully the relative importance of the various drivers, especially whether the recent changes are indeed a response to past perturbations. Acquiring the data necessary to answer this question was the motivation for recovering sediments beneath the floating part of PIG.

Three 20-cm-diameter holes were drilled through PIG ice shelf (PIG A-C) during December 2012 and January 2013 to access the ocean cavity below[18] (Fig. 1b and c). Sediment cores were recovered at each site using a hand-operated percussion corer. PIG A and C were located on the seaward flank of the prominent sea-floor ridge and PIG B was located on its landward side (Fig. 1b and c). All cores are characterised by two distinct facies (Fig. 2, Extended data Fig. 1) documenting the transition from a grounded glacier to a freely-floating ice shelf[19,20].

Facies 2 is a stratified (facies 2a) to homogenous (facies 2b) sandy-gravelly mud deposited proximal to, but not beneath, grounded ice. The unit is devoid of biogenic material. It is overlain by facies 1, a thin (4-6.5 cm) sedimentologically distinct unit of well-sorted laminated to homogenous terrigenous muds deposited beneath the ice shelf in an ocean cavity (Fig. 2). This unit contains diatom fragments of taxa typical of open ocean and sea-ice environments found in sediments from Pine Island Bay[21] (Methods). Facies 2 is produced by melt-out of material, current transport and sediment mass flows proximal to grounded ice. Such sediments have been widely documented across the Antarctic shelf, deposited during retreat of the LGM ice sheet[20,22,23].

The lack of coarse clasts in facies 1 (Fig. 2a-c) indicates deposition beneath an ice shelf at a sufficient distance from the GL not to be affected by mass flows. At this 'null zone'[20], only the finest particles supplied by plumes from the GL and those advected beneath the ice shelf from the open ocean are deposited. This interpretation is consistent with observations by Autosub that meltwater emanating from the GL carries a signature of increased light attenuation from suspended sediment[9] and the thick acoustically layered deposits in inner Pine Island Bay which increase in thickness towards the modern GL interpreted as sediment plume deposits[24].

The sedimentary sequences provide the first direct evidence for ungrounding of PIG from the transverse ridge prior to the satellite era. ^{210}Pb geochronology (Extended Data Figs. 2-3) constrains the depositions of facies 1 to 1970 ± 4 years at PIG C and to 1945 ± 12 years at PIG B. For PIG B, the ^{210}Pb age-model is further supported by measuring $^{239+240}$Pu isotopes which document the onset of widespread nuclear weapons testing in the early 1950s and its peak in the early 1960s (Extended Data Fig. 4, 5). PIG A was not dated due to insufficient material but we assume an identical age to PIG C due to their proximity and similar stratigraphy (Methods). The proposed age for the onset of fine-grained deposition at PIG C (1970 ± 4 years) is clearly supported by observational data. Satellite imagery indicates that part of PIG was still grounded on the transverse ridge until ~1973[12] and this explains why coarse-grained sediments were still deposited at sites PIG C and PIG A until the ice shelf unpinned in ~1973 (Fig. 3b). We propose that the grounded ice bulldozed sediment off the ridge crest, generating down-slope mass flows (facies 2a at PIG C and A). This process can be seen on acoustic imagery of the sea-floor under PIG which confirms that the ridge was a former pinning point, with sediment being scoured from its crest and deposited on its seaward slope[12,25]. The crude stratification in facies 2a of cores PIG C and A is consistent with this interpretation and contrasts with the homogenous and coarser composition of facies 2b in core PIG B (Fig. 2, Extended Data Fig. 1), deposited at or close to the GL. Modern process studies reveal that similar coarse-grained sediments can extend up to 1.5 km seaward of the GL[23]. These constraints place the GL to within 1.5 km when facies 2b was deposited, although the presence of pebble-sized clasts (>8 mm) within the upper part of the sequence suggests the GL was probably closer. Following unpinning of the ice shelf from this ridge in ~1973 scouring of the crest ceased, allowing fine-grained material to accumulate at PIG C and A (Fig. 3a, b).

Deposition of facies 2b at PIG B (Fig. 3a) implies there was accommodation space for the sediment to accumulate prior to 1945. We suggest that the GL started to retreat from the deeper parts of the ridge to the south of our core sites (Fig 1b) immediately prior to 1945. As the ocean cavity on the landward side of the ridge broadened to incorporate areas to the east of the high point, a small hollow was created in the N-S trending saddle landward of PIG B (Fig. 1c) providing space for coarse-grained sediment to accumulate (Fig. 3a). The lack of gradation between the two units indicates that the switch in sedimentation occurred rapidly. Assuming current retreat rates of ~1 km/yr;[2] a switch from coarse-grained GL proximal (i.e., within 1.5 km) to fine-grained deposition could have occurred in less than 2 years.

Multi-proxy data also document the change from deposition in a GL proximal setting to sediment-plume (cavity) deposition with an open marine influence (Fig. 2). The clay mineral smectite, along with bromine, which is a proxy for marine productivity[26] reflects the increasing influence of marine waters in the ocean cavity as the ice shelf unpinned and a connection across the ridge was established (Fig. 1c, Fig. 3). Smectite has no known source in the PIG catchment[27] with surface sediments indicating a dominant offshore source[27,28]. Increases in smectite and bromine – clearly observed in facies 1 – therefore reflects increasing marine influence in the ocean cavity. Such a transport pathway implies southward water mass advection across the shelf consistent with the dominant flowpath of CDW[9]. This indicates that although the ice shelf remained grounded to at least one part of the ridge in the early 1970s, ocean currents were circulating around the topographic high (Fig 1c). A similar scenario was observed in 2009 where part of the ice shelf remained grounded on a sea-floor high, with the GL located 5-10 km landward of this point[4].

Our findings have important implications for understanding the controls on ice sheet retreat. Whilst supporting the inference that PIG ice shelf finally unpinned from the transverse ridge in the early 1970s[12], we observe that the ocean cavity just inland of the seafloor ridge first opened up to ocean waters around 1945, shortly after significant El Niño conditions between 1939-42[16,17] and observed warming in West Antarctica between 1936-4517. At this time the ice was still firmly grounded on the highest parts of the ridge, where it may have been grounded since the early Holocene, but it must have lifted off towards the south to allow an ocean cavity to develop upstream of the still grounded parts (Fig. 1c); first allowing coarse-grained deposition, then as the ocean cavity enlarged and the GL retreated c.1.5 km inland of PIG B, fine-grained sediments to accumulate. The ice remained in contact with the highest parts of the ridge, bulldozing sediment off the ridge crest and down the seaward slope until the early 1970s, consistent with interpretations of the earliest Landsat imagery[12,13].

Our core data constraining the opening of an ocean cavity to 1945, provides the first quantitative support to the idea that the changes we observe currently in the Amundsen Sea were triggered by a climatic anomaly in the late 1930s to 1940s, which until now has remained largely speculative[16,29]. Despite a return to pre-1940s climatic conditions in the ensuing decades[17], thinning and glacier retreat has not stopped and is unlikely to be reversible, without a major change in marine or glaciological conditions. This indicates that a period of warming in the Antarctic shelf waters triggered a significant change in the ice sheet, via the mechanism that we see today; ocean driven thinning and retreat of ice shelves leads to inland acceleration and ice sheet thinning[3,8,30]. Significantly this also suggests that ice sheet retreat can continue even when the forcing reverts to its earlier state.

References

1 Church, J. A., P.U. Clark, A. Cazenave, J.M. Gregory, S. Jevrejeva, A. Levermann, M.A. Merrifield, G.A. Milne, R.S. Nerem, P.D. Nunn, A.J. Payne, W.T. Pfeffer, D. Stammer and A.S. Unnikrishnan. in *Climate Change 2013: The Physical Science*

Basis. Contribution of Working Group I to the Fifth Assessment Report of the Intergovernmental Panel on Climate Change (ed T.F. Stocker, D. Qin, G.-K. Plattner, M. Tignor, S.K. Allen, J. Boschung, A. Nauels, Y. Xia, V. Bex and P.M. Midgley) Ch. 13, 1137-1216 (Cambridge University Press, 2013).

2 Mouginot, J., Rignot, E. & Scheuchl, B. Sustained increase in ice discharge fromthe Amundsen Sea Embayment, West Antarctica, from 1973 to 2013. *Geophys. Res. Lett.* **41**, 1576-1584, doi:10.1002/2013gl059069 (2014).

3 Favier, L. *et al.* Retreat of Pine Island Glacier controlled by marine ice-sheet instability. *Nature Climate Change* **4**, 117-121, doi:10.1038/nclimate2094 (2014).

4 Joughin, I., Smith, B. E. & Holland, D. M. Sensitivity of 21st century sea level to ocean-induced thinning of Pine Island Glacier, Antarctica. *Geophys. Res. Lett.* **37**, doi:10.1029/2010gl044819 (2010).

5 Nitsche, F. O., Jacobs, S. S., Larter, R. D. & Gohl, K. Bathymetry of the Amundsen Sea continental shelf: Implications for geology, oceanography, and glaciology. *Geochem. Geophys. Geosyst.* **8**, doi:10.1029/2007gc001694 (2007).

6 Timmermann, R. *et al.* A consistent dataset of Antarctic ice sheet topography, cavity geometry, and global bathymetry. *Earth Syst. Sci. Data* **2**, 261-273, doi:10.5194/essd-2-261-2010 (2010).

7 Dutrieux, P. *et al.* Strong Sensitivity of Pine Island Ice-Shelf Melting to Climatic Variability. *Science* **343**, 174-178, doi:10.1126/science.1244341 (2014).

8 Pritchard, H. D. *et al.* Antarctic ice-sheet loss driven by basal melting of ice shelves. *Nature* **484**, 502-505, doi:10.1038/nature10968 (2012).

9 Jacobs, S. S., Jenkins, A., Giulivi, C. F. & Dutrieux, P. Stronger ocean circulation and increased melting under Pine Island Glacier ice shelf. *Nature Geoscience* **4**, 519-523, doi:10.1038/ngeo1188 (2011).

10 Shepherd, A., Wingham, D. & Rignot, E. Warm ocean is eroding West Antarctic Ice Sheet. *Geophys. Res. Lett.* **31**, doi:10.1029/2004gl021106 (2004)..

11 Payne, A. J., Vieli, A., Shepherd, A. P., Wingham, D. J. & Rignot, E. Recent dramatic thinning of largest West Antarctic ice stream triggered by oceans. *Geophys. Res. Lett.* **31**, doi:10.1029/2004gl021284 (2004)

12 Jenkins, A. *et al.* Observations beneath Pine Island Glacier in West Antarctica and implications for its retreat. *Nature Geoscience* **3**, 468-472, doi:10.1038/ngeo890 (2010).

13 Swithinbank, C. *et al.* Coastal-change and Glaciological Map of the Eights Coast Area, Antarctica: 1972-2001 *Geological Investigation Series Map I-2600-E, USGS* (2004).

14 Hillenbrand, C-D., Kuhn, G., Smith, J.A., Goh,l K., Graham, A.G.C., Larter, R.D., Klages, J.P., Downey, R., Moreton, S.G., Forwick, M., Vaughan, D.G. Grounding-line retreat of the West Antarctic Ice Sheet from inner Pine Island Bay. *Geology* **41**, 35-38 (2012).

15 Thoma, M., Jenkins, A., Holland, D. & Jacobs, S. Modelling Circumpolar Deep Water intrusions on the Amundsen Sea continental shelf, Antarctica. *Geophys. Res. Lett.* **35**, doi:10.1029/2008gl034939 (2008).

16 Steig, E. J., Ding, Q., Battisti, D. S. & Jenkins, A. Tropical forcing of Circumpolar Deep Water Inflow and outlet glacier thinning in the Amundsen Sea Embayment, West Antarctica. *Annals of Glaciology* **53**, 19-28, doi:10.3189/2012AoG60A110 (2012).

17 Schneider, D. P. & Steig, E. J. Ice cores record significant 1940s Antarctic warmth related to tropical climate variability. *Proc. Natl. Acad. Sci. U. S. A.* **105**, 12154-12158, doi:10.1073/pnas.0803627105 (2008).

18 Stanton, T. P. *et al.* Channelized Ice Melting in the Ocean Boundary Layer Beneath Pine Island Glacier, Antarctica. *Science* **341**, 1236-1239, doi:10.1126/science.1239373 (2013).

19 Domack, E. *et al.* Stability of the Larsen B ice shelf on the Antarctic Peninsula during the Holocene epoch. *Nature* **436**, 681-685, doi:10.1038/nature03908 (2005).

20 Domack, E. W. & Harris, P. T. A new depositional model for ice shelves, based upon sediment cores from the Ross Sea and the Mac. Robertson shelf. *Annals of Glaciology* **27**, 281-284 (1998).

21 Kellogg, D. E. & Kellogg, T. B. Microfossil distribution in modern Amundsen Sea sediments. *Mar. Micropaleontol.* **12**, 203-222, doi:10.1016/0377-8398(87)90021-1 (1987).

22 Licht, K. J., Dunbar, N. W., Andrews, J. T. & Jennings, A. E. Distinguishing subglacial till and glacial marine diamictons in the western Ross Sea, Antarctica: Implications for a last glacial maximum grounding line. *Geological Society of America Bulletin* **111**, 91-103, doi:10.1130/0016-7606(1999)111<0091:dstagm>2.3.co;2 (1999).

23 Powell, R. D., Dawber, M., McInnes, J. N. & Pyne, A. R. Observations of the grounding-line area at a floating glacier terminus. *Annals of Glaciology* **22**, 217-223 (1996).

24 Witus, A. E. *et al.* Meltwater intensive glacial retreat in polar environments and investigation of associated sediments: example from Pine Island Bay, West Antarctica. *Quat. Sci. Rev.* **85**, 99-118, doi:10.1016/j.quascirev.2013.11.021 (2014).

25 Graham, A. G. C. *et al.* Seabed corrugations beneath an Antarctic ice shelf revealed by autonomous underwater vehicle survey: Origin and implications for the history of

Pine Island Glacier. *Journal of Geophysical Research-Earth Surface* **118**, 1356-1366, doi:10.1002/jgrf.20087 (2013).

26 Ziegler, M., Jilbert, T., de lange, G. J., Lourens, L. J. & Reichart, G.-J. Bromine counts from XRF scanning as an estimate of the marine organic carbon content of sediment cores. *Geochem. Geophys. Geosyst.* **9**, doi:10.1029/2007gc001932 (2008).

27 Ehrmann, W. *et al.* Provenance changes between recent and glacial-time sediments in the Amundsen Sea embayment, West Antarctica: clay mineral assemblage evidence. *Antarct. Sci.* **23**, 471-486, doi:10.1017/s0954102011000320 (2011).

28 Hillenbrand, C. D., Grobe, H., Diekmann, B., Kuhn, G. & Futterer, D. K. Distribution of clay minerals and proxies for productivity in surface sediments of the Bellingshausen and Amundsen seas (West Antarctica) - Relation to modern environmental conditions. *Mar. Geol.* **193**, 253-271, doi:10.1016/s0025-3227(02)00659-x (2003).

29 Rignot, E. Ice-shelf changes in Pine Island Bay, Antarctica, 1947-2000. *Journal of Glaciology* **48**, 247-256, doi:10.3189/172756502781831386 (2002).

30 Joughin, I., Smith, B. E. & Medley, B. Marine Ice Sheet Collapse Potentially Under Way for the Thwaites Glacier Basin, West Antarctica. *Science* **344**, 735-738, doi:10.1126/science.1249055 (2014).

Online content Methods, along with any additional Extended Data display items and Source Data, are available in the online version of the paper; references unique to these sections appear only in the online paper.

Acknowledgements The authors acknowledge the contribution of D. Pomraning in designing and manning the hot-water drill equipment. Outstanding logistic and safety support was provided by K. Gibbon, D. Einerson, E. Steinarsson, F. McCarthy, S. Consalvi, S. King, the

PIG support camp personnel, and the NSF Antarctic support team. E. Steinarsson is especially thanked for his help with the sediment coring. This research project was supported by NSF's Office of Polar Programs under NSF grants including ANT-0732926 and ANT 0732730, funding from NASA's Cryospheric Sciences Program, New York University Abhu Dabi grant 1204, and the Natural Environment Research Council–British Antarctic Survey Polar Science for Planet Earth Program. Work at LLNL performed under Contract DE-AC52-07NA27344; LLNL-JRNL-697878.

Author contributions J.A.S, R.B, D.G.V and H.F.J.C conceived the study and M.S, M.T, T.P.S conducted the fieldwork. J.A.S and N.F are responsible for sediment core analysis and J.A.S led the writing of the paper. T.J.A measured the ^{210}Pb and ^{137}Cs and developed the age models. A.M.G measured plutonium isotopes on the PIG B core. P.D and A.J provided the bathymetric compilation, multibeam imagery and knowledge of the seafloor beneath Pine Island Glacier and C-.D.H contributed expertise on glacial sedimentology and data interpretation. W.E is responsible for clay mineral and C_{org} and N_{tot} analyses and S.C performed the XRF scanning. All authors contributed to data interpretation and writing of the manuscript.

Author Information Reprints and permissions information is available at www.nature.com/reprints. The authors declare no competing financial interests. Correspondence and requests for materials should be addressed to J.A.S (jaas@bas.ac.uk).

Figure 1. Map and location of core sites on the sea-floor ridge. **a**, Map of Antarctica (inset) and enlargement of the Amundsen Sea, showing seabed elevations[5] and grounded and floating ice shelves (light grey). The black box shows area in **b**. **b**, Seabed bathymetry (in m)

beneath Pine Island Glacier showing drill sites (red triangles; PIG A-C) along the prominent sea-floor ridge. Seabed elevations beneath the ice shelf are derived from[7] which used Autosub to correct a gravimetric inversion whilst elevations beneath grounded ice are from[6]. The grounding line is indicated by the black line and the ice shelf front by the dotted black line. **c**, Profiles along (Y-Y') and across (X-X') the ridge shown in **b** (dashed line).

Figure 2. Core logs and core data for PIG sub-ice shelf cores. a-c, simplified lithology, >2 mm (gray bars) and >8 mm (black bars) grain counts (axis label right to left), percentage of clay mineral smectite (green area), bromine (Br) area counts (grey area). Black horizontal line indicates unit boundary. **d**, X-radiographs of sub-ice shelf sediment cores illustrating the two distinct lithological units present in all three cores. The upper 4-6.5 cm is composed of mud deposited in an ocean cavity. Below this, a sequence of massive to crudely stratified sandy-gravelly mud is present documenting deposition at or close to grounded ice. The onset of fine-grained sedimentation in an ocean cavity is dated to 1970 ± 4 years in PIG C and 1945 ± 12 years in PIG B. The onset of fine-grained cavity deposition in PIG A is undated but we assume the transition between facies 2 and facies 1 also occurred in 1970 ± 4.

Figure 3. Schematic representation showing processes and sedimentation beneath the PIG ice shelf. a, pre 1945, grounding line (GL) is located within 1.5 km landward of PIG B depositing proximal sediments (facies 2b = F2b). Deposition at sites PIG C and A dominated by downslope flows (facies 2a = F2a) caused by ice shelf grounding on the ridge. **b**, ~1945-1970, formation of ocean cavity in 1945 ± 12 years and deposition of fine-grained sediment (facies 1 = F1) at PIG B, with GL located over 1.5 km landward of PIG B. Ice shelf remains partially grounded on sea-floor ridge generating downslope flows deposited at PIG C and PIG A (facies 2a). Inflow of marine water over or around ridge brings ^{210}Pb, smectite and

bromine (Br). **c**, ~1970-present, unpinning of PIG ice shelf from sea-floor ridge in 1970 ± 4 years, stopping downslope flows and enabling accumulation of fine grained sediments in PIG C and PIG A.

METHODS

Sediment cores. Sediment cores were recovered using a hand-operated UWITEC percussion corer, utilising access holes drilled during an oceanographic field campaign[18], and returned from Antarctica to the British Antarctic Survey (BAS) for analysis. Physical properties (magnetic susceptibility, wet bulk density (WBD)) were measured on whole cores using GEOTEK multisensor core loggers (MSCL) at the British Ocean Sediment Core Research Facility (BOSCORF, Southampton, UK). Magnetic susceptibility was additionally measured on the split halves of the cores using a BARTINGTON MS2F point sensor. The sediment cores were split, described and sub-sampled at BAS. Diatom content was assessed qualitatively from sediment smear slides. Individual sediment sub-samples (1 cm-thick slices) were then taken every 2-5 cm and used to determine water content, grain size, total carbon (TC), organic carbon (C_{org}) and total nitrogen (N_{tot}). C_{org} and N_{tot} were determined using a Vario EL III Elemental analyser at the Institute for Geophysics and Geology (University of Leipzig, Germany) and are used to calculate C_{org}/N_{tot}. Analytical precision was 1% for the TC measurements and 3% for the C_{org} measurements. Proportions of gravel (>2 mm), sand (63 µm to 2 mm), and mud (<63 µm) were determined on a weight basis. Gravel grains (2 mm-8 mm) and pebbles (>8 mm) were also counted on the X-radiographs at 1 cm intervals. An aliquot of the ≤2 µm fraction was used to determine the relative contents of the clay minerals smectite, illite, chlorite and kaolinite using an automated powder diffractometer system Rigaku MiniFlex with CoKα radiation (30 kV, 15 mA) at the Institute for Geophysics and Geology (University of Leipzig). The clay mineral identification and quantification followed standard X-ray diffraction methods[27].

X-ray fluorescence (XRF) measurements were carried out using an Avaatech XRF-Core Scanner at the Godwin Laboratory for Palaeoclimate Research, Department of Earth Sciences, University of Cambridge. The flat surface of the core was prepared for analysis by covering it with a 2-µm-thick Ultralene® foil. An Rh anode X-ray tube was used with a silicon drift detector (SDD) with collimation to 8 mm^2 using a silver collimator. Four powdered standards supplied by the Avaatech company (www.avaatech.com) were analysed every day prior to and after the analysis of the peat to monitor signal drift. The analysis of these four standards showed that the signal remained stable during the analytical runs. Ca, Ti, Cr, Fe, Cu, Zn, Ga, Sr, Y, Cd, Ba and Pb were detected at a resolution of 2.5 mm (2.5 mm downcore window; 12 mm across-core window). Ca, Ti, Cr and Fe were detected at 10 kV; Cu, Zn, Ga and Sr at 30 kV; and Y, Cd, Ba and Pb at 50 kV, with a sampling time of 30s at each energy level. Data were evaluated by analysis of the X-ray spectra generated at each energy level using the WIN AXIL Batchsoftware (www.canberra.com). XRF data is presented as area counts/seconds. The split core halves were X-rayed at the Department of Veterinary Medicine, University of Cambridge.

Facies classification and core correlation. Lithological units were defined on the basis of visual core description, inspection of x-radiographs, physical properties, clay mineral and XRF data. All three cores contain two distinct lithological units (Figs. 2, 3 and Extended Data Fig. 1), with unit boundaries established visually and refined using the x-radiographs and Ca/Ti ratio; the latter providing a precise measure (measured every 2.5 mm) of the change in sedimentation. The uppermost lithological unit (facies 1) in all cores consists of a 4-6.5 cm thick mainly terrigenous light olive brown (2.5YR 5/3) terrigenous mud. Faint laminations (c. 1-2 mm thick) are visible in PIG A and B. The unit is characterised by low shear strength (0 kPa), 40-50% water content, and 80-100% mud (Extended Data Fig. 1). Grains >2 mm are absent (Fig. 2). The unit contains diatom fragments (<2%) of taxa typical of open ocean and sea-ice environments (e.g., *Fragilariopsis* sp., and *Eucampia antarctica*) and consistent with surface sediments analysed from PIB[21]. Moreover, facies 1 is defined by high smectite and bromine contents as well as low C_{org}/N_{tot} ratios when compared to the underlying sediments. Bromine, exclusively associated with marine organic matter[26,31] is used here as a proxy for marine influence. Increasing marine input, relative to grounding line sedimentation is also witnessed by the accumulation of nitrogen (observed in the C_{org}/N_{tot} data), which reflects an increase in marine organic matter[32], and smectite. Increases in smectite can only reflect input from the ocean, rather than sediments sourced from PIG grounding line as there is no known source of smectite in the PIG catchment[27]. Locally smectite originates from the erosion of volcanic rocks in Ellsworth Land and western Marie Byrd Land and the surface sediment signature across the Amundsen Sea embayment is over-printed by a more dominant offshore source. Previous work[28] documented a supply from Peter I Island, an eastward supply via the Antarctic Circumpolar Current from further west (i.e. from the Ross Sea region), or a southward supply of smectite rich clay from the sub-Antarctic part of the South Pacific basin. On the basis of our multi-proxy dataset, we suggest that the uppermost unit (facies 1) was deposited by meltwater plumes in an ocean cavity beneath the ice shelf. Similar deposits have been described beneath modern[23] and palaeo ice shelves in previously glaciated areas of the continental shelf[20], including inner Pine Island Bay[24]. In addition, oceanographic measurements from the Autosub mission beneath the modern Pine Island Glacier ice shelf support the presence of suspended sediments as well as marine currents capable of fine-grained sediment suspension and transport[12].

Facies 1 is underlain by a dark grayish brown (2.5YR 4/2) purely terrigenous sandy and gravelly mud, separated by a sharp contact. PIG A and C are crudely stratified (facies 2a), indicating variations in sediment supply[22], whilst PIG B is largely homogenous (facies 2b). Coarser gravel layers occur between 17-31 cm, 60-64 cm, 71.5-78 cm and 86-92.5 cm in PIG A and between 25-30 cm in PIG C. Typically the unit is characterised by minor increases in shear strength (up to 4 kPa), magnetic susceptibility and a marked increase in sand and gravel content relative to facies 1 (Extended Data Fig. 1). Smectite and bromine content generally decrease down-core, whilst C_{org}/N_{tot} increases relative to facies 1 which is typical of glacier proximal to distal sediment transitions[33]. The sandy–gravelly sediments are likely to represent a mixture of debris flows, rain-out and meltwater-derived sediments that were deposited in a sub-ice shelf environment directly at the grounding line (facies 2b) or in proximity to grounded ice (facies 2a). Ice shelf cover is supported by a lack of marine diatoms and low organic carbon whilst a subglacial genesis is ruled out because of low shear strength and stratification[22]. Crude stratification in PIG A and C (facies 2a) indicates debris flows, which we suggest were caused by the ice shelf grounding on the seafloor ridge and bulldozing sediment downslope. Subglacial bedforms imaged on the ridge together with debris flows on its seaward side of the ridge support this interpretation[12,25]. Run-out distances of ~8 km (i.e., from the ridge crest to PIG C) are well within the measured range of coarse-grained glacigenic debris flows in other polar settings[34]. In contrast, homogenous coarse-grained sediments similar to those occurring in PIG B (facies 2b) are deposited within 1.5 km of the grounding line as modern process studies have revealed[23].

^{210}Pb dating and age models. The chronology was established by measuring the ^{210}Pb activity at the Gamma Dating Centre, Department of Geosciences and Natural Resource

Management, University of Copenhagen (Extended Data Fig. 2-3). The samples were analysed for the activity of ^{210}Pb and ^{137}Cs by way of gamma-spectrometry using Canberra ultra low-background Ge-detectors. ^{210}Pb was measured by way of its gamma-peak at 46.5 keV, ^{226}Ra by way of the granddaughter ^{214}Pb (peaks at 295 and 352keV) and ^{137}Cs by way of its peak at 661 keV. The age models are based on samples from 10 levels in PIG B and 8 levels in PIG C (between 5-15 g dry material from 0.5 cm thick levels). PIG B showed a monotonous decline in unsupported ^{210}Pb with depth which warrants the use of the CF:CS model (Constant Flux : Constant Sedimentation rate[35,36]). The age model for PIG C was calculated using the CRS-model (Constant Rate of Supply[36]) due to the irregular and non-monotonic decline with depth. Error was calculated on the basis of the standard error on the regression line[37] (CF:CS) and error-propagation (CRS) according to Appleby[38]. Asymmetric errors (CF:CS model) have been summed and averaged. The age-models, yield dates of 1945 ± 12 years and 1970 ± 4 years for the onset of fine-grained (cavity) deposition at PIG B and PIG C, respectively. We also assume an age of 1970 ± 4 years for the onset of fine-grained sedimentation at PIG A based on the core to core correlation between PIG C and PIG A, evident in the sedimentology, physical properties and XRF data (Extended Data Fig. 6). The antipathetic behaviour of Ca to Ti, and their similar behaviour to water absorption, means they are routinely used for stratigraphic correlations[39]. Similarly, the high precision and sensitivity of magnetic susceptibility loggers makes this measurement extremely reliable for core-to-core correlation[40]. Thus we are confident that the same sedimentary processes, and consequently the timing of deposition, are recorded at PIG C and A. Calculated sedimentation rates for PIG C and PIG B are 0.95 mm/yr and 0.82 mm/yr respectively. These values are comparable with sedimentation rates observed in cores recovered seaward of the modern PIG calving line (e.g., 0.86 mm/yr;[24]), interpreted to have been deposited as meltwater plumes proximal to the GL as the glacier retreated inland during deglaciation.

^{137}Cs was below detection in the majority of measured samples (detection limit for ^{137}Cs- was 2-3 Bq kg^{-1}) so cannot be used as chronostratigraphic marker. To overcome this and validate the ^{210}Pb age model we measured plutonium (Pu)-isotopes which have an identical source to ^{137}Cs, resulting from nuclear fallout, but are much longer-lived and thus remain at detectable levels in the sediment longer than ^{137}Cs.

Pu analysis. Pu analysis was performed at Lawrence Livermore National Laboratory, CA, USA. For the upper 5 cm of PIG B, pairs of sequential 0.5 cm thick sediment slices were combined to a total of five 1 cm-thick slices. Three 0.5 cm thick samples were analysed from 5 to 6.5 cm core depth in PIG B. Two samples from facies 2 were analysed as 'blank' samples, and were used to confirm the Pu detection limit for this method. Sample masses ranged from 7.1960 g to 12.0329 g.

Sediment samples were placed in quartz tubes, the tubes were plugged with quartz wool, and the sediments were thermally ashed in a muffle furnace for 12 hours at 450˚ C. Sample mass loss during ashing ranged from 1 to 2%, indicating that the samples contained only a small amount of carbonate material. Ashed samples were transferred to Teflon jars, and 20 mL of 8 M HNO_3 and ^{244}Pu tracer were added to the samples. The samples were fluxed at 125˚ C for 4 hours, and then centrifuged to separate the leachate from the leached residue. Plutonium was then chemically purified from the sample leachate. All acids used throughout the procedure are ultrapure reagents from Seastar Chemicals, Inc. The first column utilized a 2 mL anion exchange resin bed (AG1x8 100-200 mesh). The sample was loaded in 8 M HNO_3, and the column was rinsed first with 8 M HNO_3 and then 9 M HCl. Pu was eluted in a 9 M HCl + HI mixture. Next, the sample was purified on a second anion exchange column (1 mL resin bed). The sample was dissolved and loaded in 9 M HCl with trace HNO_3, the column was rinsed in 9 M HCl, and then Pu was eluted in 9 M HCl +HI. For the final purification step, the sample was loaded on a 0.6 mL resin bed of TEVA selective extraction resin (Eichrom Technologies, Inc.). The sample was dissolved and loaded in 4 M HNO_3 with trace $NaNO_2$, and the column was rinsed with 4 M HNO_3 followed by 9 M HCl. Pu was eluted with 0.1 M HCl + 0.005 M HF and then 0.1 M HCL + HI. Plutonium recovery ranged from 31% to 72%, and recoveries for most samples were between 40% and 60%.

Plutonium isotopic analyses were performed using a Nu Plasma II MC-ICP-MS instrument with an array of five electron multiplier ion counters configured specifically for Pu isotopic analysis, which enables static multi-collection of masses 239, 240, 241, 242 and 244 on ion counters. Samples were dissolved in 2% HNO_3 + 0.005 M HF for analysis, and were introduced to the instrument using a Cetac Aridus II desolvating nebulizer. The sample inlet system was rinsed between sample analyses with 5% HNO_3 + 0.05 M HF, 2% HNO_3 + 0.05 MHF and 2% HNO_3 + 0.005 M HF. Detector baselines were measured at low- and high-side half masses for 30 s, and the average intensity was subtracted from sample signal intensities. Instrumental blank measurements were measured prior to each sample, on a solution of 2% HNO_3 + 0.005 M HF. Instrumental blank measurements were corrected for detector baselines using the same method as used for sample analyses, and the baseline-corrected blank signals were subtracted from sample signals during data reduction. Sample solutions were analysed for 30 cycles of 10 s integrations. New Brunswick Laboratory certified reference material (NBL CRM) 137 was used to correct analytical results for instrumental mass bias and detector gain factors. Mass bias corrections were made assuming an exponential law. An ultra-high purity (99.98%) ^{244}Pu tracer was used for concentration determinations, so corrections to the Pu isotopic composition from spike-stripping calculations are minimal. NBL CRM 138 was measured as a quality control standard, and results for this standard measured over the course of this investigation were all consistent with the certified values for this standard. Pu concentrations were determined by isotope dilution mass spectrometry. The

Pu detection limit for this method is 0.5 fg Pu/mL of sample solution. For a sample mass of 10 g, Pu recovery of 50%, and a 3 mL analytical volume, this detection limit corresponds to 0.3 fg Pu/g sediment.

Pu-isotopes as an independent chronostratigraphic marker in marine sediments. $^{239+240}Pu$ concentration data are shown in Extended Data Fig. 4 and reveals: (1) a distinct shift from values that are below detection to values consistent with Southern Hemisphere[41] fallout at 5.25-4.5 cm (Extended Data Figure 4, panel c); (2) $^{239+240}Pu$ concentrations are near-uniform above this transition. According to our ^{210}Pb age-model, the observed increase in $^{239+240}Pu$ (at 5.25 cm) occurs at 1951 ± 12, increasing to 5.8 fg/g (equivalent to 0.01905 Bq/kg) by 1960 ± 6 (at 4.5 cm) (Extended Data Fig. 4a, b). Nuclear weapons testing was conducted from 1945-1980. Radionuclides were additionally released during the Chernobyl accident in 1986 but are not typically detected in the Southern Hemisphere. Peak 'atmospheric' fallout is observed between 1952 and 1956 in Antarctic ice cores[42,43] whilst the highest overall concentrations of Pu fallout in Antarctica has been recorded in the nearby Thwaites and Pine Island Glacier catchment (Extended Data Fig. 5)[43].

The $^{239+240}Pu$ data from PIG B clearly show the onset of widespread nuclear weapons testing in the early 1950s, and thereby provide independent validation for the ^{210}Pb age model. Whilst the peak concentration for $^{239+240}Pu$ is clearly delineated in our dataset and agrees with the expected date/depth of maximum fallout, a clear feature of the Pu data is that values then remain largely constant throughout facies 1. We suggest that this reflects the longer residence time of Pu in the ocean compared to the atmosphere. Many marine sediment cores for which a Pu stratigraphy has been determined are taken from areas very close to land such as estuaries and bays. These locations all have a significant terrigenous input, and do not reflect an isolated polar marine environment where a component of fallout is locked-up in the ice sheet. Furthermore, the PIG B sediments show that the marine residence time of Pu, as recorded in the Amundsen Sea, is long enough to buffer the Pu deposition rate so that there are not the large Pu peaks that are observed in ice cores. Highest concentrations of Pu in the world's ocean are observed in the Pacific[44] which is one of the major source waters for CDW (together with the Indian and North Atlantic oceans). Here, and in other areas, Pu profiles are characterised by a typical surface minimum and sub-surface maxima between 500-1500 m. Importantly, the Pu concentration in the mid and deep ocean has been maintained at nearly constant levels since enrichment in the 1950/60s (measurements between 1973-2001[45]) and in some areas (e.g., North Pacific) might have increased with depth as the sub-surface Pu maximum has deepened. Therefore, although the overall input of Pu to the world's ocean has declined significantly in the last four decades, the long half-life and chemical properties of Pu mean that it has persisted in the main source areas for CDW at levels similar to pre and post moratorium levels[44]. Thus the dominance of CDW on the Amundsen Sea shelf and below PIG, which still has a Pu concentration close to fallout levels, explains the observed profile in PIG B.

Data availability. Bedrock topography used in Fig. 1a can be obtained from http://www.marine-geo.org/link/entry.php?id=Amundsen_Sea_Nitsche whilst seabed elevation beneath the ice shelf (Fig. 1b and c) are derived from the previously published compilation of Dutrieux *et a*l.[7]. All sedimentological data, including core logs and X-radiographs as well as tabulated grain-size, shear strength, water content, Br area counts, Ca/Ti and C_{tot}/N_{tot} data shown in Fig. 2 and Extended Data Fig. 1 and 6, in addition to ^{210}Pb, ^{137}Cs and Pu-isotope data in Extended Data Fig. 2, 3 and 4 are available from the corresponding author. Antarctic ice-core data (^{239}Pu) in Extended Data Fig. 5 are available from NSF Arctic Data Center (https://arcticdata.io/) and for the J-9 ice core in tabulated form in Koide *et al.*[42].

31 Mayer, L. M., Schick, L. L., Allison, M. A., Ruttenberg, K. C. & Bentley, S. J. Marine vs. terrigenous organic matter in Louisiana coastal sediments: The uses of bromine: organic carbon ratios. *Marine Chemistry* **107**, 244-254, doi:10.1016/j.marchem.2007.07.007 (2007).

32 Meyers, P. A. Organic geochemical proxies of paleoceanographic, paleolimnologic, and paleoclimatic processes. *Org. Geochem.* **27**, 213-250 (1997).

33 Smith, J. A. *et al.* New constraints on the timing of West Antarctic Ice Sheet retreat in the eastern Amundsen Sea since the Last Glacial Maximum. *Glob. Planet. Change* **122**, 224-237, doi:10.1016/j.gloplacha.2014.07.015 (2014).

34 Laberg, J. S. & Vorren, T. O. Flow behaviour of the submarine glacigenic debris flows on the Bear Island Trough Mouth Fan, western Barents Sea. *Sedimentology* **47**, 1105-1117, doi:10.1046/j.1365-3091.2000.00343.x (2000).

35 Brush, G. S., Martin, E. A., Defries, R. S. & Rice, C. A. Comparisons of ^{210}Pb and pollen methods for determining rates of estuarine sediment accumulation. *Quat. Res.* **18**, 196-217, doi:10.1016/0033-5894(82)90070-9 (1982).

36 Appleby, P. G. & Oldfield, F. The assessment of 210Pb data from sites with varying sediment accumulation rates. *Hydrobiologia* **103**, 29-35 (1983).

37 Appleby, P. G., Jones, V. J. & Ellis-Evans, J. C. Radiometric Dating of Lake-Sediments from Signy Island (Maritime Antarctic) - Evidence of Recent Climatic-Change. *J. Paleolimn.* **13**, 179-191 (1995).

38 Appleby, P. G. Chronostratigraphic techniques in recent sediments, in *Tracking Environmental Change Using Lake Sediments Volume 1: Basin Analysis, Coring, and*

Chronological Techniques (eds W.M. Last & J.P. Smol) 171-203 (Kluwer Academic, 2001).

39 Hennekam, R. & de Lange, G. X-ray fluorescence core scanning of wet marine sediments: methods to improve quality and reproducibility of high-resolution paleoenvironmental records. *Limnology and Oceanography Methods* **10**, 991-1003 (2012).

40 Verosub, K. L. & Roberts, A. P. nvironmental magnetism – Past, present and future. *J. Geophys. Res.-Solid Earth* **100**, 2175-2192, doi:10.1029/94jb02713 (1995).

41 Kelley, J. M., Bond, L. A. & Beasley, T. M. Global distribution of Pu isotopes and 237Np. *Science of the Total Environment* **237–238**, 483-500, doi:http://dx.doi.org/10.1016/S0048-9697(99)00160-6 (1999).

42 Koide, M., Bertine, K. K., Chow, T. J. & Goldberg, E. D. The Pu-240 Pu-239 Ratio, a Potential Geochronometer. *Earth Planet. Sci. Lett.* **72**, 1-8, doi: 10.1016/0012-821x(85)90112-8 (1985).

43 Arienzo, M. M. *et al.* A Method for Continuous (PU)-P-239 Determinations in Arctic and Antarctic Ice Cores. *Environmental Science & Technology* **50**, 7066-7073, doi:10.1021/acs.est.6b01108 (2016).

44 Lindahl, P., Lee, S. H., Worsfold, P. & Keith-Roach, M. Plutonium isotopes as tracers for ocean processes: A review. *Marine Environmental Research* **69**, 73-84, doi:10.1016/j.marenvres.2009.08.002 (2010).

45 Livingston, H. D., Povinec, P. P., Ito, T. & Togawa, O. in *Plutonium in the Environment. Radioactivity in the Environment, Vol. 1* (ed A. Kudo) 267-292 (Elsevier, 2001).

Extended Data Figure 1. Core logs and core data for PIG sub-ice shelf cores. a-c, Simplified lithology, shear strength (closed black squares), water content (open squares), contents of mud (0-63 µm; black fill), sand (63 µm-2 mm; dark grey fill) and gravel (>2 mm; light grey fill), magnetic susceptibility (measured with a MS2F surface probe; red line), smectite, bromine (Br) area counts and C_{org}/N_{tot}. Facies classification is shown on the right of the panel. Facies 1 is sedimentological distinct from facies 2, and the measured parameters are consistent in all cores. Dashed horizontal line indicates the unit boundary.

Extended Data Figure 2. **^{210}Pb and ^{137}Cs activities as a function of depth. a**, PIG C. **b**, PIG B. Error bars denote 2 standard deviations of ^{210}Pb and ^{137}Cs concentrations. Note that concentration of ^{137}C is at or below detection limit throughout both cores. **c**, Constant rate of Supply (CRS) modelling of down-core profile of $^{210}Pb_{xs}$ in the PIG C core. Black line marks regression to calculate ^{210}Pb concentration below 7 cm. **d**, Constant flux: Constant sedimentation (CF:CS) of down-core $^{210}Pb_{xs}$ concentrations in the PIG B core. Regression used to calculate the CF:CS chronology for PIG B. Solid dots: data used in the regression, open dots: data not used in the regression.

Extended Data Figure 3. **Age-depth models calculated using regression in Extended Data Fig. 2**. **a**, PIG C. **b**, PIG B. Horizontal dashed line represent unit boundary between facies 1 and facies 2. Error bars calculated on the basis of error-propagation[35] (PIG C) and the error on the regression line[38] (PIG B) (see Methods).

Extended Data Figure 4. Plutonium-isotope data. a Depth profile of Plutonium concentrations in PIG B (expanded uncertainty is given for the 95% confidence interval in panel **c**). The abrupt increase in $^{239+240}$Pu between 5.25 cm and 4.5 cm from levels below detection (b.d.l) equates to between 1951 ± 12 and 1960 ± 6 according to the age model which is consistent with peak fallout recorded in Antarctica (1952-1956[42,43]; Extended Data Fig. 5) as well as the global peak observed in 1963. **b** $^{239+240}$Pu plotted against ^{210}Pb age-model (age uncertainty derived from the standard error of the linear regression). The dotted horizontal line marks the transition between facies 1 and facies 2. **c** $^{239Pu/240}$Pu in PIG B is consistent with Southern Hemisphere average $^{239Pu/240}$Pu fallout = 0.185 ± 0.047[41]. Expanded Uncertainty is given for the 95% confidence interval; b.d.l. is below detection limit of 0.5 fg Pu/mL of sample solution. Activity is calculated for sediment dry weight, using the following half-lives: ^{239}Pu $t_{1/2}$ = 24,110 years; ^{240}Pu $t_{1/2}$ = 6,563 years.

Extended Data Figure 5. **Relative $^{239+240}$Pu concentrations for Antarctic ice cores**. Grey bars represent the J-9 ice core[42], located on the Ross Ice Shelf. Peak $^{239+240}$Pu concentrations are observed between 1952 and 1956. Black line represents a recent composite of 6 Antarctic ice cores, including ice cores from Pine Island (red line) and Thwaites Glaciers (blue line)[43].

Extended Data Figure 6. Core to core correlation between PIG C (red line) and PIG A (black line). a, Ca/Ti. **b**, Magnetic susceptibility (MS). Values have been offset to highlight correlation. The concurrent changes in physical data, matched also by sedimentological changes combined with the proximity of the two cores implies that the transition from coarse to fine-grained sedimentation likely occurred at the same time.

Figure 1

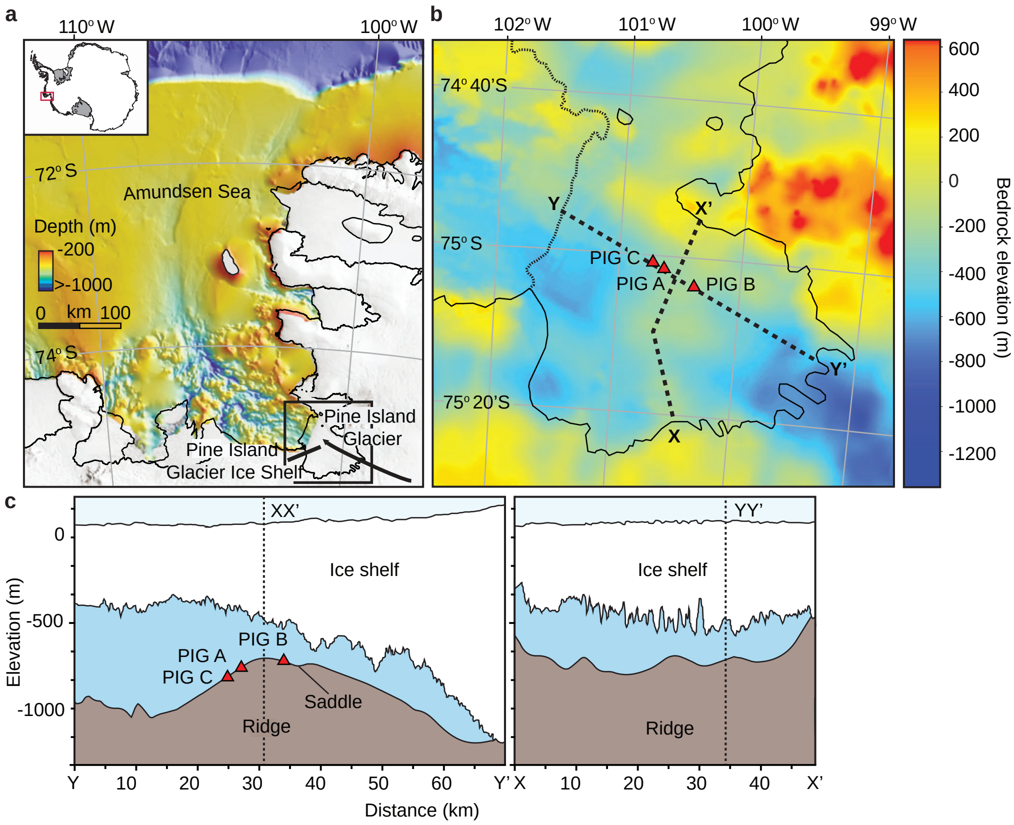

a
110° W
100° W
72° S
Amundsen Sea
Depth (m)
-200
>-1000
0 km 100
74° S
Pine Island Glacier
Pine Island Glacier Ice Shelf
b
102° W
101° W
100° W
99° W
74° 40'S
75° S
75° 20'S
Y
X'
PIG C
PIG A
PIG B
Y'
X
600
400
200
0
-200
-400
-600
-800
-1000
-1200
Bedrock elevation (m)
c
XX'
0
Ice shelf
Elevation (m)
-500
PIG B
PIG A
PIG C
Saddle
-1000
Ridge
Y 10 20 30 40 50 60 Y'
Distance (km)
YY'
Ice shelf
Ridge
X 10 20 30 40 X'

Figure 2

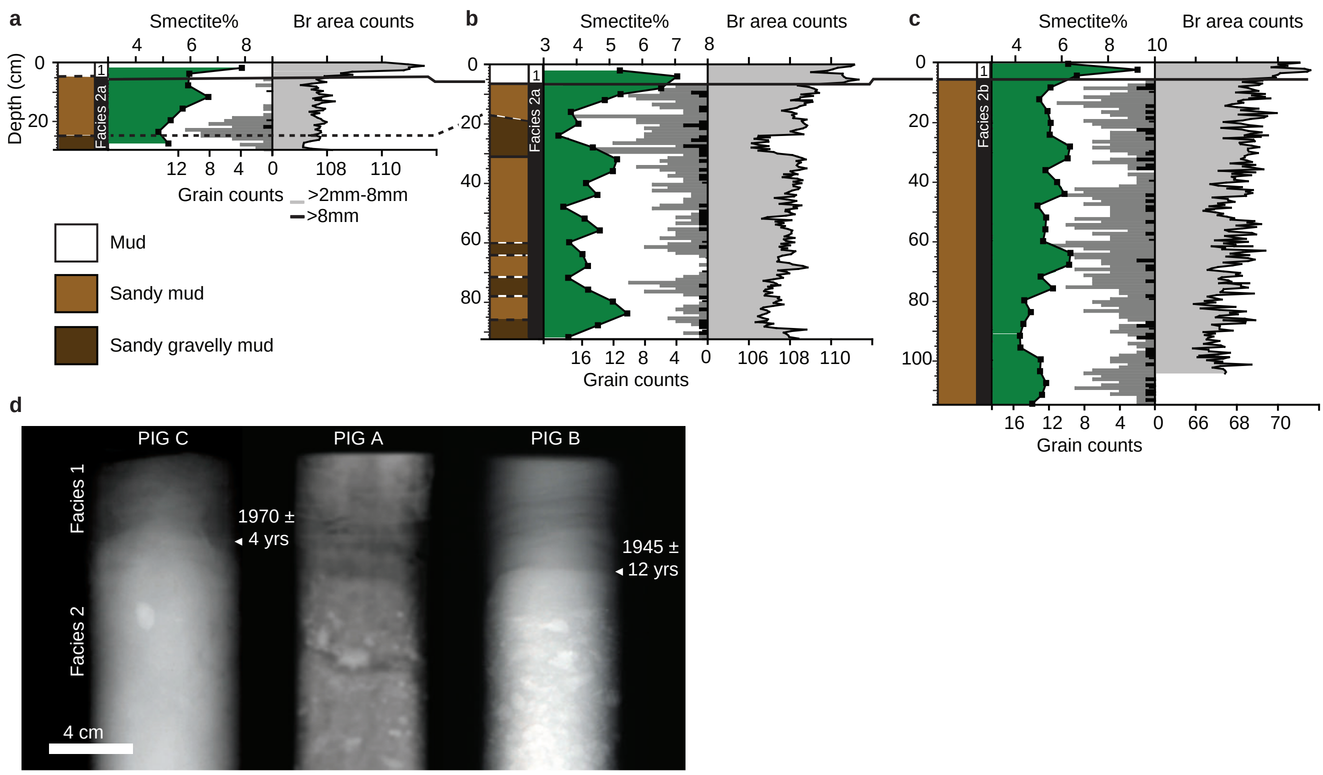

a
Smectite%
4 6 8
Br area counts
Depth (cm)
0
20
1
Facies 2a
12 8 4 0
108 110
Grain counts
>2mm-8mm
>8mm
Mud
Sandy mud
Sandy gravelly mud
b
Smectite%
3 4 5 6 7 8
Br area counts
0
20
40
60
80
1
Facies 2a
16 12 8 4 0
106 108 110
Grain counts
c
Smectite%
4 6 8 10
Br area counts
0
20
40
60
80
100
1
Facies 2b
16 12 8 4 0
66 68 70
Grain counts
d
PIG C
PIG A
PIG B
Facies 1
Facies 2
1970 ± 4 yrs
1945 ± 12 yrs
4 cm

Figure 3

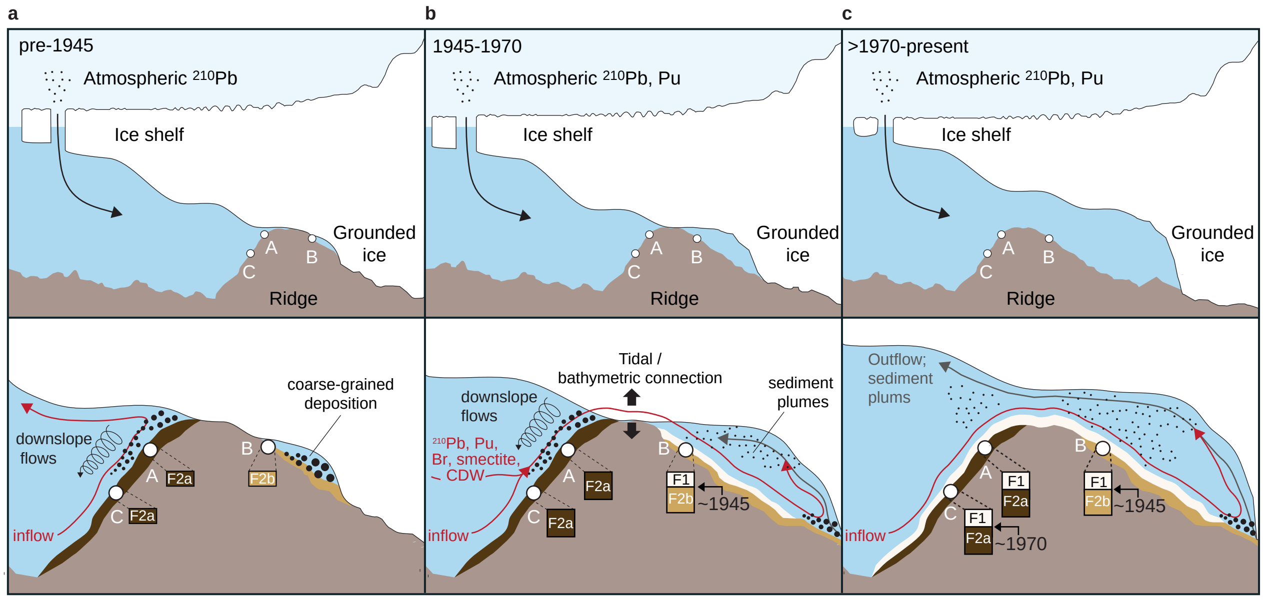
a
b
c
pre-1945
Atmospheric 210Pb
Ice shelf
Grounded ice
Ridge
A
B
C
1945-1970
Atmospheric 210Pb, Pu
>1970-present
downslope flows
coarse-grained deposition
inflow
F2a
F2b
Tidal / bathymetric connection
sediment plumes
210Pb, Pu, Br, smectite, CDW
F1
~1945
Outflow; sediment plums
~1970